Status update on point spread function reconstruction algorithm development for laser guide star multi-conjugate adaptive optics

L. Gilles[1a], L. Wang[a], C. Boyer[a]
[a]Thirty Meter Telescope International Observatory LLC, 100 W. Walnut St, Pasadena, CA 91124, USA;

ABSTRACT

This paper provides a status update on point spread function reconstruction (PSFR) algorithm development for laser guide star (LGS) multi-conjugate adaptive optics (MCAO). The PSFR algorithm works in Fourier space and reconstructs the system optical transfer function (OTF), which is the Fourier transform of the system PSF. The Multithreaded Adaptive Optics Simulator (MAOS), configured to simulate the Thirty Meter Telescope (TMT) Narrow Field InfraRed Adaptive Optics System (NFIRAOS) feeding the InfraRed Imaging Spectrograph (IRIS), provided system OTFs and real time controller (RTC) telemetry data. The following five topics are addressed in this paper: (1) the variability of the PSF from one exposure to another for a given stationary frozen flow turbulence condition (constant r_0) and a given exposure time, which places a fundamental limit on PSFR accuracy, (2) the reconstruction of the system OTF degradation due to LGS wavefront sensor (WFS) measurement noise in absence of turbulence, (3) the reconstruction of the system OTF degradation due to LGS WFS measurement noise in presence of turbulence, (4) the impact of a slope detection and ranging (SLODAR) turbulence profile estimation error on PSFR accuracy, and (5) the reconstruction of the system OTF degradation due to static telescope errors using a measured PSF on the sky in the presence of LGS WFS measurement noise, servo-lag and residual turbulence.

Keywords: Laser guide star multi-conjugate adaptive optics (LGS MCAO), point spread function reconstruction (PSFR)

1. INTRODUCTION

Point spread function reconstruction (PSFR) has gained increased attention in the adaptive optics (AO) community with the design and construction of extremely large telescopes (ELTs) [1]-[9]. In this paper, laser guide star (LGS) multi-conjugate adaptive optics (MCAO) PSFR algorithm developments are presented for the Thirty Meter Telescope (TMT) first-light LGS MCAO system, NFIRAOS, feeding the InfraRed Imaging Spectrograph (IRIS). An overview of NFIRAOS is provided in [13] and of IRIS in [14] and [15]. The PSFR algorithm works in Fourier space and reconstructs the system optical transfer function (OTF), which is the Fourier transform of the system PSF. To perform this OTF reconstruction, an OTF is computed from an end-to-end simulation model, and is multiplied by a correction filter expressed as the ratio of a long-exposure OTF computed from the system de-noised actuator error covariance matrix to another long-exposure OTF computed from the simulated model de-noised actuator error covariance matrix. The end-to-end simulation is fed by the following system real time controller (RTC) telemetry data: (1) the high-order (HO) and low-order (LO) MCAO control matrices, (2) the deformable mirror (DM) poke matrix (from which the actuator influence functions can be estimated), (3) the HO and LO temporally averaged subaperture images and signal levels, (3) the estimate of the turbulence profile obtained from a slope detection and ranging (SLODAR) algorithm [16] running concurrently with the MCAO science observation. The correction filter is estimated using the following system and simulation model RTC telemetry data: (1) the actuator error covariance matrix (which includes both HO and LO modes), (2) the HO and LO wavefront sensor (WFS) gradient noise covariance matrices. Finally, in order to estimate the system OTF degradation due to static telescope aberrations, an on-sky PSF measurement is required.

As a reminder, the short-exposure (SE) PSF in the optical system (telescope + MCAO relay + instrument) focal plane (FP) and short-exposure OTF in the optical system exit pupil (XP) are related to the optical field in the XP under far field scalar diffraction theory as follows [17]:

[1] lgilles@caltech.edu; phone 1-626-395-1622

$$
\begin{aligned}
&\mathrm{PSF}^{\mathrm{SE}}(\vec{x}_{\mathrm{FP}}) = \frac{\left|\mathcal{F}\{U_{\mathrm{XP}}(\vec{x}_{\mathrm{EP}})\}_{\vec{f}_{\mathrm{EP}}=\vec{x}_{\mathrm{FP}}/(\lambda f_{\mathrm{E}})}\right|^2}{\left[\mathcal{F}\{U_{\mathrm{DL}}(\vec{x}_{\mathrm{EP}})\}_{\vec{f}_{\mathrm{EP}}=\vec{0}}\right]^2} = \frac{\left|\mathcal{F}\{U_{\mathrm{XP}}(\vec{x}_{\mathrm{EP}})\}\right|^2}{\left[\int d^2\vec{x}_{\mathrm{EP}} U_{\mathrm{DL}}(\vec{x}_{\mathrm{EP}})\right]^2} \geq 0, \\
&U_{\mathrm{XP}}(\vec{x}_{\mathrm{EP}}) = U_{\mathrm{DL}}(\vec{x}_{\mathrm{EP}}) \exp\{i \cdot k \cdot \mathrm{OPD}_{\mathrm{XP}}(\vec{x}_{\mathrm{EP}})\}, \\
&OTF^{\mathrm{SE}}(\vec{f}_{\mathrm{FP}}) = \frac{\int d^2\vec{x}_{\mathrm{EP}} U_{\mathrm{XP}}(\vec{x}_{\mathrm{EP}}) U_{\mathrm{XP}}{}^*(\vec{x}_{\mathrm{EP}} + \lambda f_{\mathrm{E}} \vec{f}_{\mathrm{FP}})}{\int d^2\vec{x}_{\mathrm{EP}} \left[U_{\mathrm{DL}}(\vec{x}_{\mathrm{EP}})\right]^2}
\end{aligned}
\tag{1.1}
$$

where $\vec{x}_{\mathrm{FP}}$ denotes the 2D spatial coordinate in the FP, $\vec{f}_{\mathrm{FP}}$ denotes the 2D spatial frequency coordinate in the FP conjugate of $\vec{x}_{\mathrm{FP}}$, $\mathcal{F}\{\cdot\}$ denotes the 2D Fourier transform operator, $U_{\mathrm{DL}}(\vec{x}_{\mathrm{EP}})$ is the real-valued amplitude function at spatial coordinate $\vec{x}_{\mathrm{EP}}$ in the entrance pupil (EP), $U_{\mathrm{XP}}(\vec{x}_{\mathrm{EP}})$ is the XP optical field expressed as a function of EP spatial coordinates $\vec{x}_{\mathrm{EP}}$, $k = 2\pi/\lambda$ is the wavenumber, λ is the imaging wavelength, $\mathrm{OPD}_{\mathrm{XP}}(\vec{x}_{\mathrm{EP}})$ is the XP optical path difference expressed as a function of EP spatial coordinates. For an object at infinity at an object-space angular coordinate $\vec{\theta}_{\text{Obj-EP}}$, $\vec{x}_{\mathrm{FP}}$ is expressed as follows:

$$
\vec{x}_{\mathrm{FP}} = f_{\mathrm{E}} \cdot \tan(\vec{\theta}_{\text{Obj-EP}}) \tag{1.2}
$$

and $f_{\mathrm{E}} \vec{f}_{\mathrm{FP}}$ is the conjugate variable of $\tan(\vec{\theta}_{\text{Obj-EP}})$. Under the small angle approximation, $\tan(\vec{\theta}_{\text{Obj-EP}}) \simeq \vec{\theta}_{\text{Obj-EP}}$ (the error is 1% for $\vec{\theta}_{\text{Obj-EP}} = 10$ deg, hence the approximation is accurate for astronomical objects). The full width at half maximum of the Airy disk is equal to $\mathrm{FWHM}_{\mathrm{Airy}} = \lambda f_\#$, where $f_\#$ is the optical system focal ratio, and the PSF is Nyquist sampled if it is sampled at resolution $\Delta x_{\mathrm{FP}} = \lambda f_\# / 2$.

In the long-exposure (LE) limit (i.e. when speckle patterns have averaged out), $OTF^{\mathrm{SE}}(\vec{f}_{\mathrm{FP}})$ in (1.1) becomes:

$$
OTF(\vec{f}_{\mathrm{FP}}) = \frac{\mathcal{F}\{\mathrm{PSF}(\vec{x}_{\mathrm{FP}})\}}{\int d^2\vec{x}_{\mathrm{FP}} \mathrm{PSF}(\vec{x}_{\mathrm{FP}})} = \frac{\int d^2\vec{x}_{\mathrm{EP}} U_{\mathrm{DL}}(\vec{x}_{\mathrm{EP}}) U_{\mathrm{DL}}(\vec{x}_{\mathrm{EP}} + \lambda f_{\mathrm{E}} \vec{f}_{\mathrm{FP}}) \exp\left[-\frac{k^2}{2} \mathrm{SF}_{\mathrm{XP}}(\vec{x}_{\mathrm{EP}}, \vec{x}_{\mathrm{EP}} + \lambda f_{\mathrm{E}} \vec{f}_{\mathrm{FP}})\right]}{\int d^2\vec{x}_{\mathrm{EP}} \left[U_{\mathrm{DL}}(\vec{x}_{\mathrm{EP}})\right]^2}, \tag{1.3}
$$

where the temporal average symbol $\langle\cdot\rangle$ on the OTF and PSF has been omitted for simplicity, $\mathrm{SF}_{\mathrm{XP}}(\vec{x}_{\mathrm{EP}}, \vec{x}_{\mathrm{EP}}')$ denotes the XP OPD structure function (SF), i.e. the variance of the differential XP OPD between points $\vec{x}_{\mathrm{EP}}$ and $\vec{x}_{\mathrm{EP}}'$ in the EP. The LE PSF is obtained by taking the inverse Fourier transform of (1.3):

$$
\mathrm{PSF}(\vec{x}_{\mathrm{FP}}) = \mathcal{F}^{-1}\left\{OTF(\vec{f}_{\mathrm{FP}})\right\} \int d^2\vec{x}_{\mathrm{FP}} \mathrm{PSF}(\vec{x}_{\mathrm{FP}}) \tag{1.4}
$$

(1.3) is discretized as follows:

$$
OTF(\vec{f}_{\mathrm{FP,(j)}}) = \frac{\sum_i U_{\mathrm{DL}}(\vec{x}_{\mathrm{EP,(i)}}) \cdot U_{\mathrm{DL}}(\vec{x}_{\mathrm{EP,(i)}} + \lambda f_{\mathrm{E}} \vec{f}_{\mathrm{FP,(j)}}) \cdot \exp\left[-\frac{k^2}{2} \mathrm{SF}_{\mathrm{XP}}(\vec{x}_{\mathrm{EP,(i)}}, \vec{x}_{\mathrm{EP,(i)}} + \lambda f_{\mathrm{E}} \vec{f}_{\mathrm{FP,(j)}})\right]}{\sum_i \left[U_{\mathrm{DL}}(x_{\mathrm{EP}(i)})\right]^2}, \tag{1.5}
$$

where $\vec{f}_{\mathrm{FP,(j)}}$ denotes the j^{th} spatial frequency vector in the FP sampled on a grid of resolution $\Delta f_{\mathrm{FP}} = \lambda f_{\mathrm{E}} \Delta x_{\mathrm{EP}}$, where Δx_{EP} is the spatial sampling in the EP and $\vec{x}_{\mathrm{EP,(i)}}$ is the spatial coordinate vector of the i^{th} grid point in the EP, $\mathrm{SF}_{\mathrm{XP}}(\vec{x}_{\mathrm{EP,(i)}}, \vec{x}_{\mathrm{EP,(i')}})$ denotes the XP OPD SF matrix element at row i and column i', which is related to the XP OPD covariance matrix C as follows:

$$
\mathrm{SF}_{\mathrm{XP}}(\vec{x}_{\mathrm{EP,(i)}}, \vec{x}_{\mathrm{EP,(i')}}) \equiv \mathrm{SF}_{ii'} = C_{ii} + C_{i'i'} - 2C_{ii'} \tag{1.6}
$$

A schematic block diagram of the PSFR algorithm is provided in Figure 1. The system OTF is estimated as a product of transfer functions (TFs) (which is an approximation ignoring the cross-coupling between wavefront error terms [18]) as follows:

$$
\begin{aligned}
&OTF_{\text{AtmosTur+Impl}}(\vec{\theta}_{\text{sc}},\zeta,\varphi,T_{\text{sc}},T_{\text{calTel}},T_{\text{calAO}},T_{\text{calIns}}) = \hat{K}_{\text{Impl}}(\vec{\theta}_{\text{sc}},\zeta,\varphi,T_{\text{calTel}},T_{\text{calAO}},T_{\text{calIns}})\cdot OTF_{\text{AtmosTur}}(\vec{\theta}_{\text{sc}},\zeta,\varphi,T_{\text{sc}}) \\
&\hat{K}_{\text{Impl}}(\vec{\theta}_{\text{sc}},\zeta,\varphi,T_{\text{calTel}},T_{\text{calAO}},T_{\text{calIns}}) = \hat{K}_{\text{Impl,Tel}}(\vec{\theta}_{\text{sc}},\zeta,\varphi,T_{\text{calTel}})\cdot\hat{K}_{\text{Impl,AO}}(\vec{\theta}_{\text{sc}},\varphi,T_{\text{calAO}})\cdot\hat{K}_{\text{Impl,Ins}}(\vec{\theta}_{\text{sc}},\varphi,T_{\text{calIns}})
\end{aligned}
\tag{1.7}
$$

where $\hat{K}_{\text{Impl}}(\vec{\theta}_{\text{sc}},\zeta,\varphi,T_{\text{calTel}},T_{\text{calAO}},T_{\text{calIns}})$ denotes the implementation error TF for a science target at angular coordinate $\vec{\theta}_{\text{Obj-FP}} = \vec{\theta}_{\text{sc}}$ in object space, zenith angle ζ, pupil rotation angle φ, decomposed into telescope (Tel), AO and instrument (Ins) implementation errors measured at times $T_{\text{calTel}},T_{\text{calAO}},T_{\text{calIns}}$ respectively, and $OTF_{\text{AtmosTur}}(\vec{\theta}_{\text{sc}},\zeta,\varphi,T_{\text{sc}})$ denotes the TF accounting for the OTF degradation due to the combined effects of residual turbulence, measurement noise and servo-lag for a science observation at time T_{sc}.

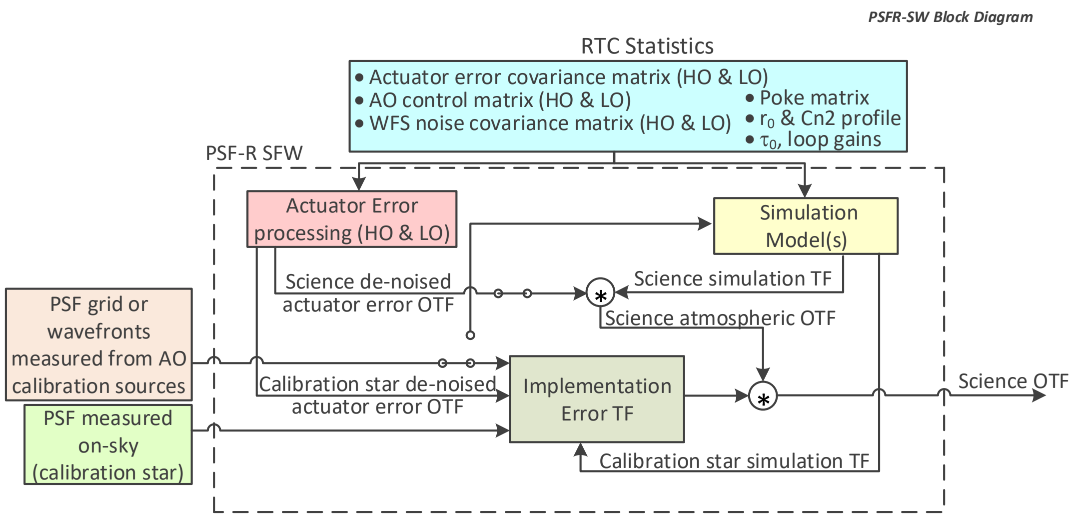

Figure 1: Block diagram of the PSFR algorithm.

Since telescope implementation errors (telescope mirrors figure errors after alignment and phasing system (APS) correction [19] are mostly field independent, the calibration can be performed for a given telescope pointing and pupil angle using an on-sky PSF measurement anywhere in the MCAO field of regard. The telescope implementation error TF is computed as follows:

$$
\begin{aligned}
\hat{K}_{\text{Impl,Tel}}(\vec{\theta}_{\text{sc}},\zeta,\varphi,T_{\text{calTel}},T_{\text{calAO}},T_{\text{calIns}}) &\simeq \hat{K}_{\text{Impl,Tel}}(\vec{\theta}_{\text{cal}},\zeta,\varphi,T_{\text{calTel}},T_{\text{calAO}},T_{\text{calIns}}) \\
&= \frac{OTF_{\text{AtmosTur+Impl}}(\vec{\theta}_{\text{cal}},\zeta,\varphi,T_{\text{calTel}})}{\hat{K}_{\text{Impl,AO}}(\vec{\theta}_{\text{cal}},\varphi,T_{\text{calAO}})\cdot\hat{K}_{\text{Impl,Ins}}(\vec{\theta}_{\text{cal}},\varphi,T_{\text{calIns}})\cdot OTF_{\text{AtmosTur}}(\vec{\theta}_{\text{cal}},\zeta,\varphi,T_{\text{calTel}})}
\end{aligned}
\tag{1.8}
$$

where $\vec{\theta}_{\text{cal}}$ denotes the calibration star coordinate on the sky and $OTF_{\text{AtmosTur+Impl}}(\vec{\theta}_{\text{cal}},\zeta,\varphi,T_{\text{calTel}})$ the calibration OTF measured at time T_{calTel}. If no calibration measurements are performed, $\hat{K}_{\text{Impl}} = I$ (array of ones) in (1.7). $OTF_{\text{AtmosTur}}(\vec{\theta}_{\text{sc}},\zeta,\varphi,T_{\text{sc}})$ in (1.7) and $OTF_{\text{AtmosTur}}(\vec{\theta}_{\text{cal}},\zeta,\varphi,T_{\text{calTel}})$ in (1.8) are computed as the product of an end-to-end simulation OTF excluding implementation errors, multiplied by the estimate of a correction filter accounting for sensed deviations between system and simulation model (i.e. model errors):

$$
OTF_{\text{AtmosTur}} = OTF^{\text{Sim}}\cdot\hat{K}_0(\Delta C,\Delta C^{\text{Sim}}) \tag{1.9}
$$

where OTF^{Sim} denotes the end-to-end simulation model OTF, $\hat{K}_0$ the estimate of the correction filter, ΔC the de-noised system actuator error covariance matrix estimate and ΔC^{Sim} the de-noised simulation model actuator error covariance matrix estimate, computed in post-processing as follows:

$$\begin{aligned} &\Delta C = H_a \Delta C_{\mathrm{ea}} H_{\mathrm{a}}^T, \quad \Delta C^{\mathrm{Sim}} = H_a \Delta C_{\mathrm{ea}}^{\mathrm{Sim}} H_{\mathrm{a}}^T \\ &\Delta C_{\mathrm{ea}} = C_{\mathrm{ea}} - C_{\mathrm{ean}} \xrightarrow[\mathrm{nfr}\to\infty]{} C_{\mathrm{eanf}}, \qquad \Delta C_{\mathrm{ea}}^{\mathrm{Sim}} = C_{\mathrm{ea}}^{\mathrm{Sim}} - C_{\mathrm{ean}}^{\mathrm{Sim}} \xrightarrow[\mathrm{nfr}\to\infty]{} C_{\mathrm{eanf}}^{\mathrm{Sim}} \end{aligned} \tag{1.10}$$

where H_a is the raytracing matrix along the science direction or the calibration measurement direction from actuator space to the aperture-plane wavefront reconstruction grid sampled at half the ground DM actuator pitch, C_{ea} is the actuator error covariance matrix, and C_{ean} the actuator error noise covariance matrix. The actuator error is computed by the RTC from closed-loop WFS gradients as follows:

$$\begin{aligned} \mathrm{ea} &= \mathrm{ea}_{\mathrm{HO}} + \mathrm{ea}_{\mathrm{LO}} \\ \mathrm{ea}_{\mathrm{HO}} &= (I - MM^{\dagger})\left[R_{\mathrm{HO}}^{\mathrm{RTC}} g_{\mathrm{HO}}^{\mathrm{CL}} + \delta_{\mathrm{HO}}^{\mathrm{RTC}}\right] \quad , \quad \mathrm{ea}_{\mathrm{LO}} = R_{\mathrm{LO}}^{\mathrm{RTC}} g_{\mathrm{LO}}^{\mathrm{CL}} \\ \delta_{\mathrm{HO}}^{\mathrm{RTC}} &= (R_{\mathrm{HO}}^{\mathrm{RTC}} G_a - I) a_{\mathrm{HO}} \end{aligned} \tag{1.11}$$

where $g_{\mathrm{HO}}^{\mathrm{CL}} = g_{\mathrm{HO,NF}}^{\mathrm{CL}} + \eta_{\mathrm{HO}}$ is the HO WFS closed-loop (CL) gradient vector, η_{HO} is the HO WFS measurement noise, $R_{\mathrm{HO}}^{\mathrm{RTC}}$ the RTC HO control matrix (which may include an extrapolation matrix commanding slaved actuators), $\delta_{\mathrm{HO}}^{\mathrm{RTC}}$ the RTC HO WFS gradient pseudo open-loop (POL) correction applied when $R_{\mathrm{HO}}^{\mathrm{RTC}}$ is an open-loop minimum variance control matrix and the HO loop runs using POL control, $g_{\mathrm{LO}}^{\mathrm{CL}} = g_{\mathrm{LO,NF}}^{\mathrm{CL}} + \eta_{\mathrm{LO}}$ is the LO WFS CL gradient vector, η_{LO} is the LO WFS measurement noise, $I - MM^{\dagger}$ projects out LO modes from the HO component of the actuator error, and a_{HO} is the HO component of the DM commands. The actuator error covariance matrix is computed from the actuator error time history as follows:

$$C_{\mathrm{ea}} = \left\langle (\mathrm{ea} - \left\langle \mathrm{ea} \right\rangle) \cdot (\mathrm{ea} - \left\langle \mathrm{ea} \right\rangle)^T \right\rangle \tag{1.12}$$

where $\langle \cdot \rangle$ denotes temporal averaging over all frames recorded during the science or calibration measurement exposure. The actuator error noise covariance matrix is computed in post-processing as follows:

$$\begin{aligned} C_{\mathrm{ean}} &= C_{\mathrm{ean,HO}} + C_{\mathrm{ean,LO}} \\ C_{\mathrm{ean,HO}} &= (I - MM^{\dagger}) \cdot R_{\mathrm{HO}}^{\mathrm{RTC}} C_{\mathrm{gnHO}} \left(R_{\mathrm{HO}}^{\mathrm{RTC}}\right)^T \cdot (I - MM^{\dagger})^T \\ C_{\mathrm{ean,LO}} &= R_{\mathrm{LO}}^{\mathrm{RTC}} C_{\mathrm{gnLO}} \left(R_{\mathrm{LO}}^{\mathrm{RTC}}\right)^T \end{aligned} \tag{1.13}$$

where C_{gnHO} and C_{gnLO} are the HO and LO WFS gradient noise covariance matrices retrieved from RTC telemetry data, which depend on the chosen centroiding algorithm, signal level and detector read-out noise. In the limit of an infinite number of frames, ΔC_{ea} approaches the actuator error covariance matrix computed from noise-free gradients $g_{\mathrm{HO,NF}}^{\mathrm{CL}}$ and $g_{\mathrm{LO,NF}}^{\mathrm{CL}}$ in (1.11). The correction filter estimate $\hat{K}_0$ in (1.9) is computed from the system and simulation model actuator error covariance matrices, and takes one of the following three forms, denoted Est1, Est2, Est3 respectively:

$$\hat{K}_0(\Delta C, \Delta C^{\mathrm{Sim}}) = \begin{cases} I \quad [\mathrm{Est1}] \\ \mathrm{Upsamp}\left\{OTF\left(\Delta C\right) / OTF\left(\Delta C^{\mathrm{Sim}}\right)\right\} \quad [\mathrm{Est2}] \\ \mathrm{Upsamp}\left\{OTF\left(\Delta C - \Delta C^{\mathrm{Sim}}\right) / OTF_{\mathrm{DL}}\right\} \quad [\mathrm{Est3}] \end{cases} \tag{1.14}$$

Est1 does not use actuator error telemetry and is a simple identity filter (array of ones), whereas Est2 and Est3 are OTF ratios, $OTF\left(\Delta C\right)$ denotes the long-exposure OTF computed from ΔC using (1.5) and (1.6), and $\mathrm{Upsamp}\{\cdot\}$ up-samples the filters to finer resolution using bilinear splines. OTF_{AtmosTur} in (1.9) estimates OTF_{AtmosTur} exactly provided the model is error-free. In the presence of model errors (which always occur in practice), the estimation error is given by:

$$\frac{OTF_{\text{AtmosTur}}}{OTF_{\text{AtmosTur}}} = \frac{K_0}{\hat{K}_0}, \qquad K_0 = \frac{OTF_{\text{AtmosTur}}}{OTF^{\text{Sim}}} \tag{1.15}$$

where $\hat{K}_0$ is given in (1.14) and K_0 is the ideal correction filter yielding a zero estimation error.

2. SIMULATION RESULTS

2.1 Geometry parameters and PSFR metrics

All simulations were performed using the Multi-threaded adaptive optics simulator (MAOS) [20], the TMT telescope model (entrance pupil diameter $D_{\text{EP}} = 30$ m), and the default NFIRAOS parameters [21]. The main simulation parameters are: TMT segmented aperture, six HO laser guide stars (LGSs) (five on a 70'' diameter pentagon plus one on-axis), order 60 x 60 Shack-Hartman LGS WFSs running at 800 Hz, 1 tip/tilt/focus (TTF) and 1 tip/tilt (TT) natural guide stars (NGSs) forming an equilateral triangle of 20'' width centered on-axis, one deformable mirror (DM) of order 63 x 63 conjugate to ground, a second DM of order 76 x 76 conjugate to 11.8 km, 30% inter-actuator coupling (IAC), Nyquist sampled Z-band ($\lambda_Z = 880$ nm) PSFs (Nyquist sampling in Z-band is $\Delta\theta_{\text{Obj-EP}} = \lambda_Z / (2D_{\text{EP}}) \simeq 3\,\text{mas}$) sampled on a 3 x 3 grid partitioning the IRIS imager 34'' x 34'' field of view (FoV) centered on-axis, all OPDs computed on grids sampled at (1/64) m. The 7,000 x 32,000 MCAO minimum variance control matrix, $R_{\text{HO}}^{\text{RTC}}$ in (1.11) and (1.13), is pre-computed offline using 100 iterations of the Fourier Domain Preconditioned Conjugate Gradient (FDPCG) algorithm for the tomography component and Cholesky back solves for the DM fitting component [21]. Six LO modes (tip/tilt/focus and 3 plate-scale modes) are controlled separately from the HO modes using the split atmospheric tomography architecture [22]. 30 sec exposures (24,000 frames at 800 Hz) are simulated with 256 m wide translating atmospheric phase screens sampled at (1/64) m with a 30 m turbulence outer scale.

PSFR accuracy is assessed using the following three performance metrics:

1) Strehl Ratio (SR) error: $\epsilon\text{SR} = \dfrac{\text{SR(PSF)} - \text{SR(PSF)}}{\text{SR(PSF)}}$, where PSF denotes the system PSF, PSF denotes the reconstructed system PSF, and SR is computed by taking the ratio of the PSF peak intensity to that of the modeled Diffraction Limited (DL) PSF of the same total flux.

2) Ensquared energy (EE) error: $\epsilon\text{EE}(\Omega) = \dfrac{\text{EE}(\text{PSF},\Omega) - \text{EE}(\text{PSF},\Omega)}{\text{EE}(\text{PSF},\Omega)}$, where ensquared energy is computed by Fourier shifting PSF and PSF to have their centroid at origin (center of the array) and summing pixel values over a square array Ω centered at the PSF centroid coordinate and normalizing by the total flux of the PSF: $\text{EE}(\text{PSF},\Omega) = \dfrac{\sum_{i,j\in\Omega} \text{PSF}_{i,j}}{\sum_{i,j\in\Omega_{\max}} \text{PSF}_{i,j}} \le 1$

3) PSF profile error, defined as the spatial standard deviation of the PSF estimation error relative to the system PSF standard deviation: $\epsilon Q = \sqrt{\text{FVU}}$, where FVU denotes Fraction of Variance Unexplained [23] and is given by $\text{FVU} = \dfrac{\text{var}\left\{\text{PSF} - \text{PSF}\right\}}{\text{var}\left\{\text{PSF}\right\}}$ with $\text{var}\left\{\text{PSF}\right\} = \text{Mean}\left\{\left(\text{PSF-Mean}\left\{\text{PSF}\right\}\right)^2\right\}$, where PSF and PSF are Fourier shifted to have their centroid at the origin.

2.2 PSF variability exposure to exposure under stationary frozen flow turbulence conditions

PSF variability exposure to exposure under stationary frozen flow turbulence conditions places a fundamental limit on PSFR accuracy. For TMT NFIRAOS feeding IRIS (34'' x 34'' FoV in object space) and for stationary median turbulence conditions (7 frozen flow turbulence layers characterized by $r_0 = 18.6$ cm, $\theta_0 = 2.3$'', $\theta_2 = 8.9$", $f_G = 21$ Hz, $L_0 = 30$ m) and for 30 sec exposures, the Z-band ($\lambda = 880$ nm) SR variability is on the order of 0.4% on-axis, 0.6% at mid vertices and 1.5% at IRIS field corners as illustrated in Figure 2. This level of PSF variability exposure to exposure places a fundamental limit on PSFR accuracy.

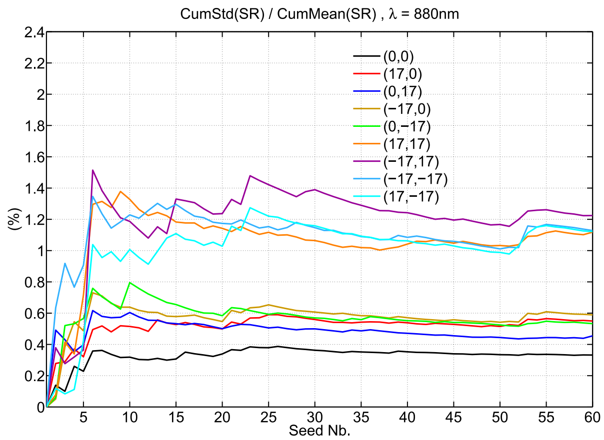

Figure 2: Cumulative standard deviation of the science PSF SR relative to its cumulative mean versus turbulence realization.

2.3 Reconstruction of the OTF degradation due to LGS WFS noise in absence of turbulence

In order to demonstrate that Est1 and Est2 in (1.14) reconstruct accurately the system OTF degradation due to LGS WFS noise (non-uniform measurement noise due to LGS perspective elongation for NFIRAOS [24]) and servo-lag, the NFIRAOS system is simulated in closed-loop at 800 Hz without atmospheric turbulence but with a low LGS WFS signal level of 225 photo-detected electrons (PDEs) per frame and per subaperture, an unoptimized integrator gain of 0.5 and a minimum variance control matrix tuned for this signal level and commanding the 2 DMs using pseudo open-loop (POL) control (i.e. with the POL correction $\delta_{\mathrm{HO}}^{\mathrm{RTC}}$ in (1.11) is applied). We intentionally impose an LGS WS signal level error in the end-to-end simulation model computing $\mathrm{Est1} = OTF^{\mathrm{Sim}}$ in (1.9) by simulating a LGS WFS signal level of 900 PDEs per frame and per subaperture but with the system control matrix tuned for 225 PDEs. PSFR results for the on-axis field are given in Figure 3, Figure 4 and Figure 5, illustrating the excellent reconstruction accuracy achieved by the Est2 and Est3 algorithms (50X reduction in all three figures of merit compared to Est1). Results over the 3 x 3 field points partitioning the IRIS 34'' x 34'' FoV are given in Figure 6 and Figure 7, indicating that the estimation error remains below 1% in Z-band ($\lambda = 880$ nm) and is field independent.

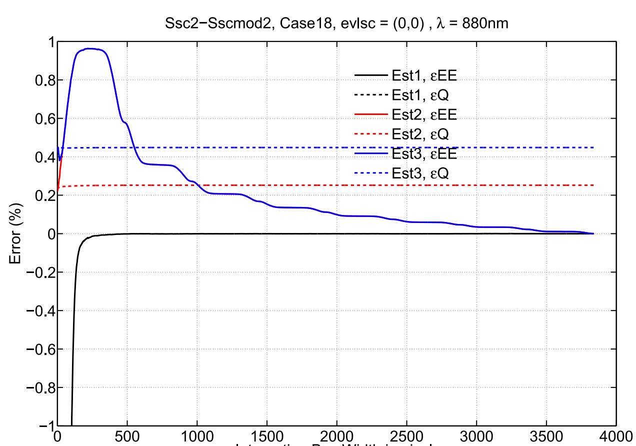

Figure 3: Left: EE curves for the on-axis field. Right: SR error (ϵSR), maximum EE error (ϵEE) and PSF profile error (ϵQ) for the on-axis field.

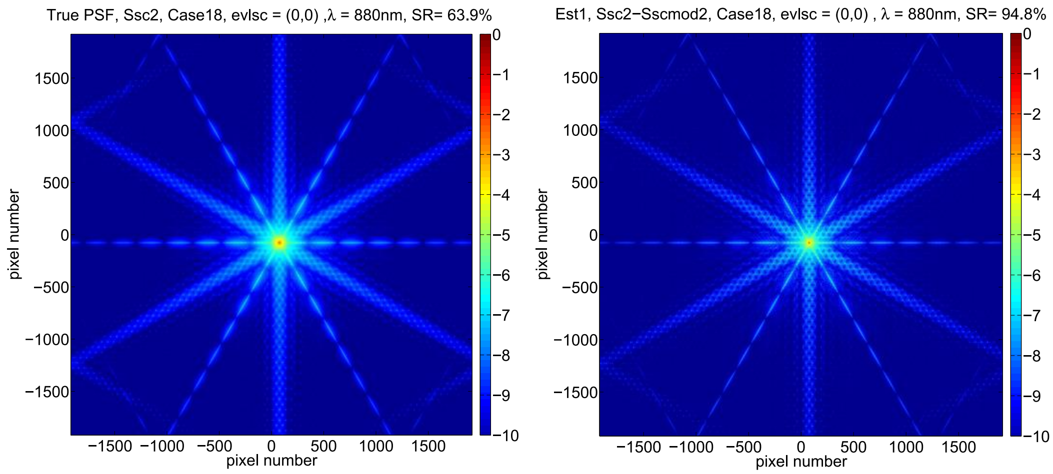

Figure 4: Left: system PSF (225 PDEs LGS WFS signal level). Right: Est1 PSF (900 PDEs LGS WFS signal level). Log10 scale.

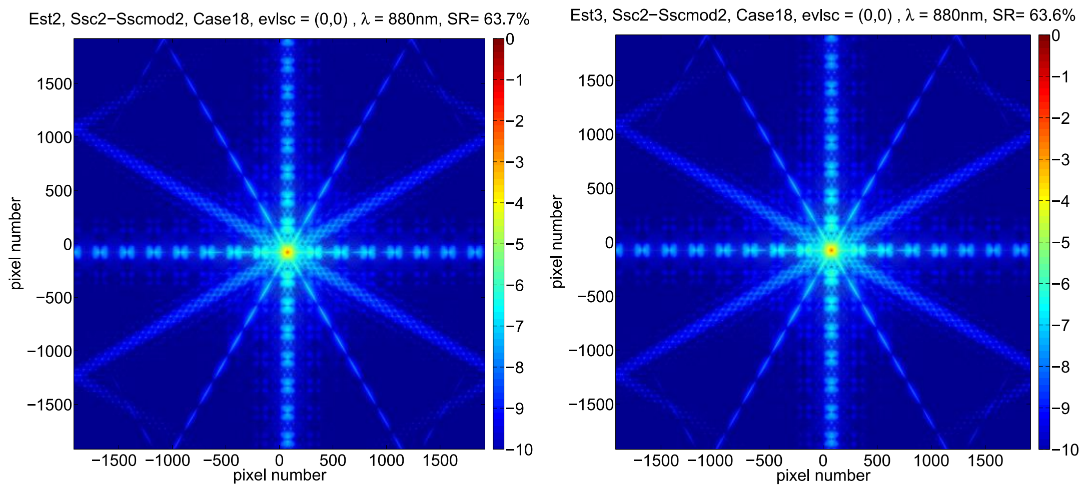

Figure 5: Left: reconstructed system PSF by the Est2 algorithm. Right: reconstructed system PSF by the Est3 algorithm. Log10 scale.

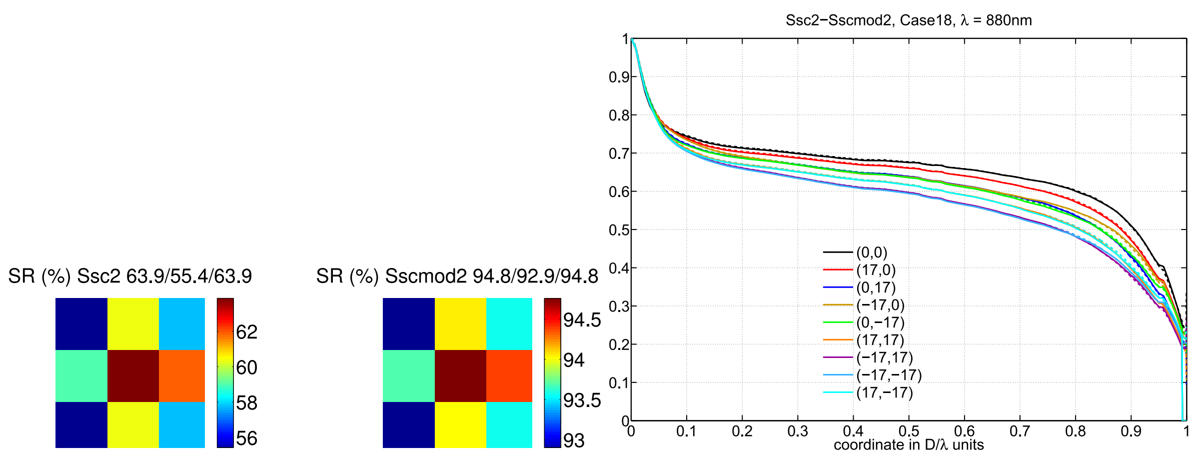

Figure 6: Left: Z-band SR at the 3 x 3 fields partitioning the 34'' x 34'' IRIS FoV (left image is for the system, right image is for the 900 PDE simulation model, and the three numbers in the title are the on-axis/min/max SR values across the 9 field points) (the origin is at the center, the (17'', 17'') coordinate is at the upper right corner, the (-17'', -17'') coordinate is at the lower left corner). Right: estimated correction filter $\hat{K}_0$ (solid curves) and ideal correction filter K_0 (dashed curves) in (1.15) for each field point.

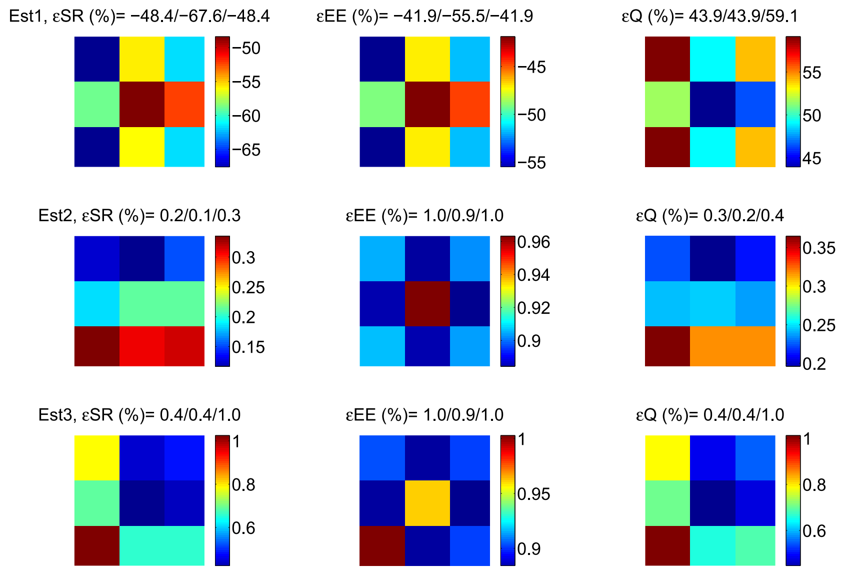

Figure 7: Z-band SR, EE and PSF profile errors for Est1, Est2 and Est3 for the 3 x 3 fields partitioning the 34'' x 34'' IRIS FoV.

2.4 Reconstruction of the OTF degradation due to LGS WFS noise in presence of turbulence

In order to determine if the excellent reconstruction accuracy of Section 2.3 holds in presence of turbulence, the experiment of Section 2.3 is repeated with the 7 frozen flow atmospheric phase screens of Section 2.2. Results are shown in Figure 8 and Figure 9. The reconstruction error becomes field dependent and has increased to 1.7% on-axis and 5.4% at field corners (10X reduction in all three figures of merit from the Est1 errors). Figure 8 indicates that the estimated correction filter $\hat{K}_0$ is too strong, particularly off-axis. Averaging PSFs and covariance matrices over multiple exposures does not reduce the estimation error, which suggests that the error must be due to correlations between measurement noise and aliasing/tomography which are not sensed by the AO system and are therefore not captured in the actuator error telemetry. Figure 10 and Figure 11 show that using a simulation model control matrix tuned for the simulation model 900 PDE LGS WFS signal level increases the PSFR errors to about 17% on-axis and 4% at field corners.

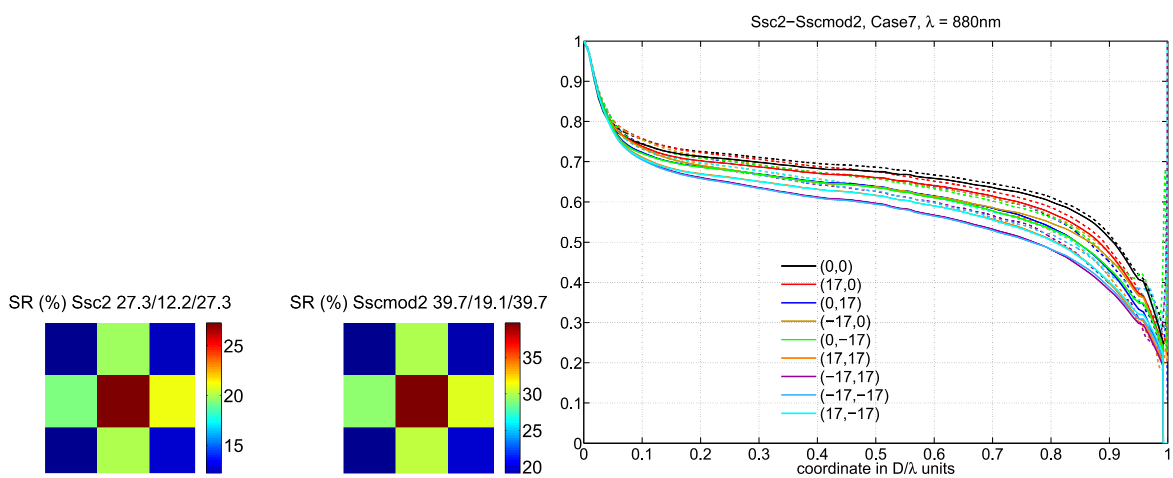

Figure 8: Left: Z-band SR at the 3 x 3 fields partitioning the 34'' x 34'' IRIS FoV (left image is for the system, right image is for the simulation model, and the three numbers in the title are the on-axis/min/max values across the 9 field points). Right: estimated correction filter $\hat{K}_0$ (solid curves) and ideal correction filter K_0 (dashed curves) in (1.15) for each field point.

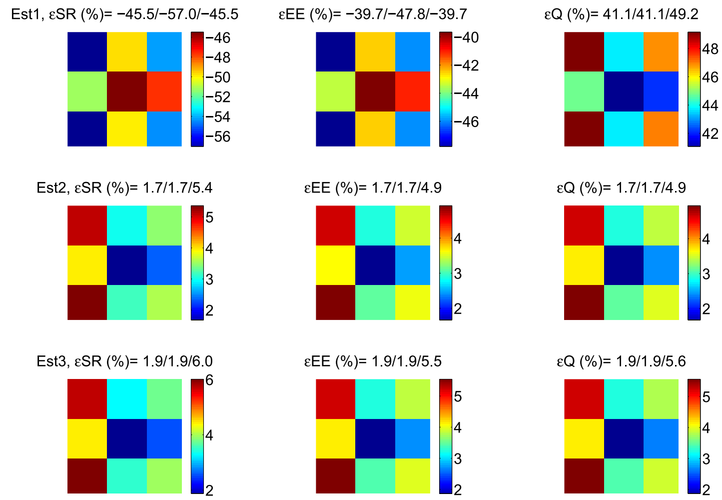

Figure 9: Z-band SR, EE and PSF profile errors for Est1, Est2, Est3 for the 3 x 3 fields partitioning the 34’’ x 34’’ IRIS FoV.

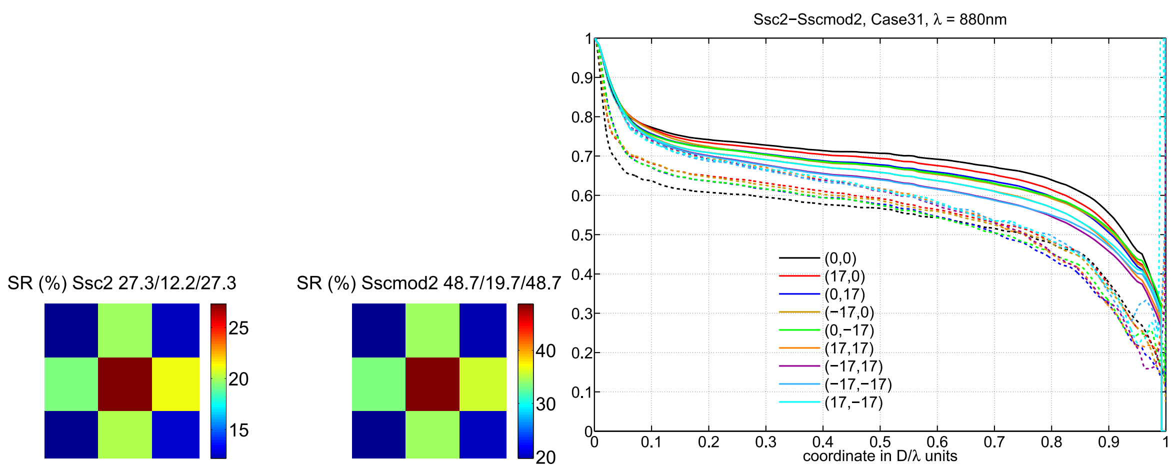

Figure 10: Same as Figure 8 but for a simulation model control matrix tuned for the simulation model 900 PDE LGS WFS signal level.

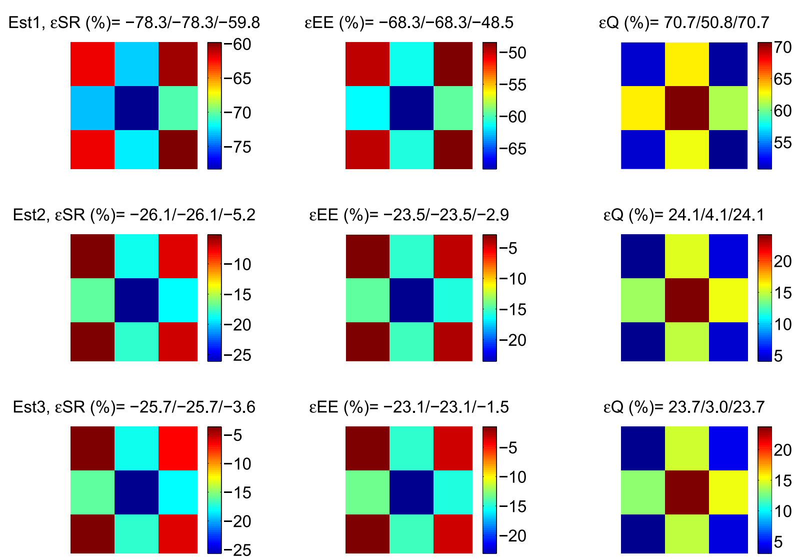

Figure 11: Same as Figure 10 but for a simulation model control matrix tuned for the simulation model 900 PDE LGS WFS signal level.

2.5 Impact of a SLODAR turbulence profile estimation error on PSFR accuracy

Accurate knowledge of the turbulence profile is critical for PSFR. In order to assess the impact of a slope detection and ranging (SLODAR) [16] turbulence profile estimation error, three profiles are simulated and PSFR is performed using the SLODAR estimates obtained concurrently with the 30 sec MCAO observation using the LGS pair of the NFIRAOS asterism separated by $\Delta\theta_{\mathrm{LGS}} = 66.7''$ along the X direction and providing a turbulence strength estimate at the following 13 non-equidistant SLODAR natural altitudes above ground-level $h_k = k\Delta / \left[\Delta\theta_{\mathrm{LGS}} + k\Delta / H\right]$ where $\Delta = 0.5$ m is the LGS WFS subaperture size projected onto the EP and $H = 90$km is the altitude of the LGS centroid in the mesosphere: 0 km, 1.523 km, 2.995 km, 4.419 km, 5.797 km, 7.131 km, 8.425 km, 9.6778 km, 10.893 km, 12.072 km, 13.216 km, 14.327 km, 15.407 km. The three profiles and the SLODAR estimates are shown in Figure 12. A layer is kept provided its weight $\omega_k = r_{0,k}^{-5/3} / r_0^{-5/3}$ is at least 1% of the largest weight (all weights sum to 1). p1 is an 11-layer profile with 1,500 m altitude sampling with layers ranging in altitude from 0 km to 15 km, p2 is a 23-layer profile with 750 m sampling with layers ranging from 0 km to 16.5 km, and p3 is a 49-layer profile with 300 m sampling with layers ranging from 0 km to 14.4 km. All three profiles are scaled to yield a Fried parameter $r_0 = 18.6$ cm at $\lambda = 500$ nm. The estimation error in r_0 is 3% for p1 and 4% for p2 and p3, the error in θ_0 is 13% for p1, 7% for p2 and 10% for p3, and the error in θ_2 is 8% for p1, 6% for p2 and 7% for p3. Averaging over the other 4 LGS pairs separated by $\Delta\theta_{\mathrm{LGS}} = 66.7''$ does not reduce the estimation error.

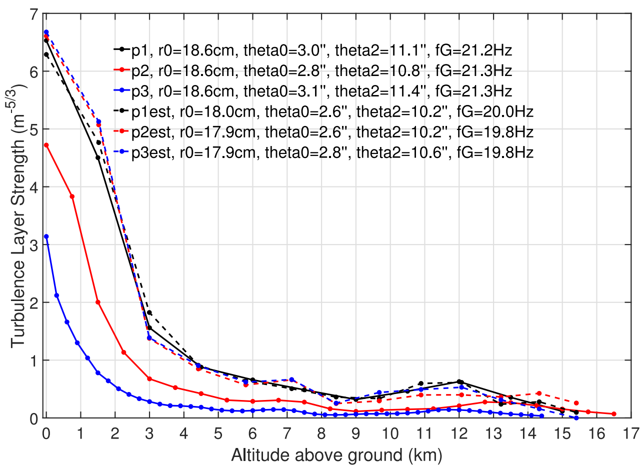

Figure 12: Turbulence profiles p1, p2, p3 (solid curves) used for the system simulation and SLODAR estimates p1est, p2est, p3est (dashed curves) used by the PSFR end-to-end simulation model. Plot shows strength $p_k = r_{0,k}^{-5/3}$ of turbulence layer k at altitude h_k above ground-level.

Since a turbulence profile estimation error is unsensed by the AO system (it impacts DM fitting, projection and tomography wavefront errors), results are given only for Est1 (identical results are obtained with Est2 and Est3). System and simulation model use the same MCAO control matrix tuned for a 6-layer turbulence profile obtained by binning the SLODAR 13-layer estimate (which preserves r_0) to the following altitudes: 0 km, 1 km, 2 km, 4 km, 8 km, 16 km. Results for p1 are given in Figure 13, and indicate 8% error on-axis and 16.6% error at field corners for all three metrics in Z-band. Similar results are obtained for p2 and p3 as shown in Figure 14 and Figure 15. The larger PSR error off-axis is due to projection and tomography errors. More accurate SLODAR turbulence profile estimates are required to reduce those PSFR errors.

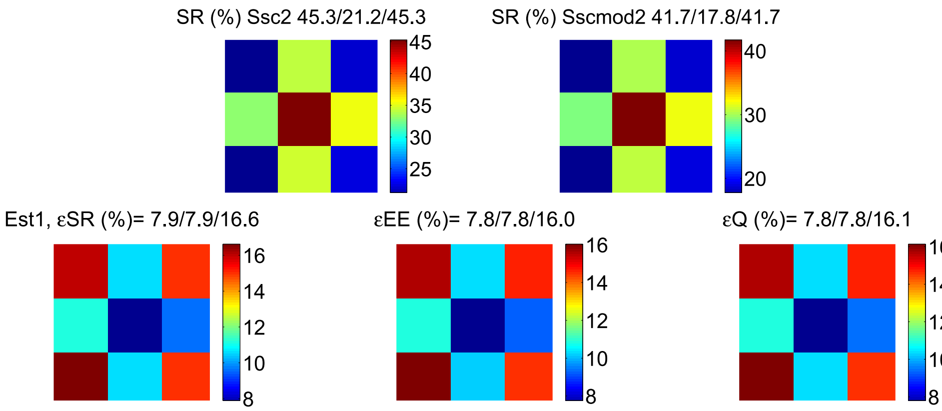

Figure 13: Top: Z-band SR at the 3 x 3 fields partitioning the 34'' x 34'' IRIS FoV (left image is for the system exposed to the p1 turbulence profile, right image is for the simulation model using the SLODAR turbulence profile estimate p1est, and the three numbers in the title are the on-axis/min/max values across the 9 field points). Bottom: Z-band SR, EE and PSF profile errors for the 3 x 3 fields partitioning the FoV.

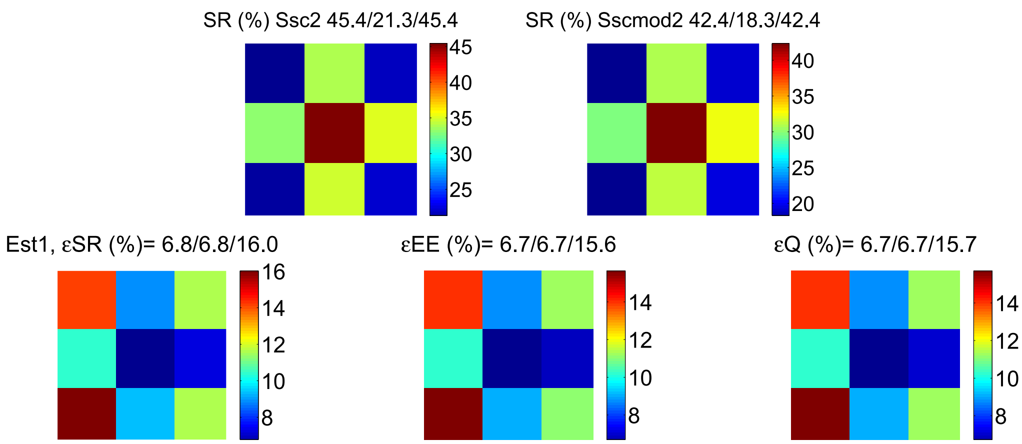

Figure 14: Same as Figure 13 but for turbulence profile p2.

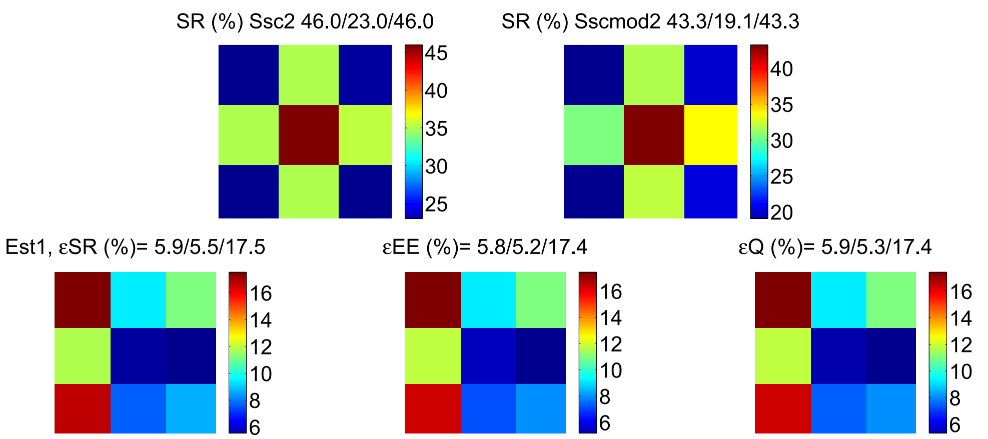

Figure 15: Same as Figure 13 but for turbulence profile p3.

2.6 Reconstruction of the OTF degradation due to static telescope errors

The final set of results discussed in this paper is on the reconstruction of the system OTF degradation due to static telescope errors in the presence of LGS WFS measurement noise, servo-lag and residual turbulence. To perform this reconstruction, an on-sky PSF measurement is performed at a different time than the science observation, and $\hat{K}_{\mathrm{Impl,Tel}}$ is estimated using (1.8). Sample TMT M1/M2/M3 OPDs are shown in Figure 16. Primary mirror (M1, which is the TMT aperture stop) errors include segment passive support error, warping harness figuring error, APS phasing error, thermal segment distortion and gravity segment clocking/decenter error. Secondary mirror (M2) errors include passive support error, figuring error and APS alignment error. Tertiary mirror (M3) errors include passive support error and figuring error. The 7-layer frozen flow atmospheric turbulence profile of Section 2.2 ($r_0 = 18.6$ cm, $\theta_0 =$ 2.3'', $\theta_2 = 8.9$'' , $f_G = 21$ Hz, $L_0 = 30$ m) and the M1/M2/M3 OPDs are used to compute the MCAO system OTF averaged over 24,000 frames at 800 Hz (30 sec exposure) and the same setup is used by the simulation model computing OTF^{Sim}, except that the M1/M2/M3 OPDs are not included. A nominal LGS WFS signal level of 900 PDEs is adopted. In order to assess the OTF degradation due to the combined M1/M2/M3 OPDs, results are given in Figure 17 ignoring the calibration measurement, i.e. $\hat{K}_{\mathrm{Impl}} = I$ (array of ones) in (1.1). All three errors are on the order of 4.3% in Z-band and are very weakly field dependent since M2 and M3 are not conjugated to high altitudes. Figure 18 shows a calibration PSF at coordinate (17'', -17'') including the effects of LGS WFS noise, servo-lag, residual turbulence and telescope errors, and the associated model excluding the telescope errors. The turbulence condition at the time of the calibration measurement is characterized by $r_0 = 13.5$ cm, $\theta_0 = 1.8$'', $\theta_2 = 6.8$'', $f_G = 29$ Hz, $L_0 = 30$ m. Figure 19 shows the Z-band PSFR errors when the calibration PSF is used to estimate the OTF degradation due to the telescope OPDs. The error in on the order of 0.6%.

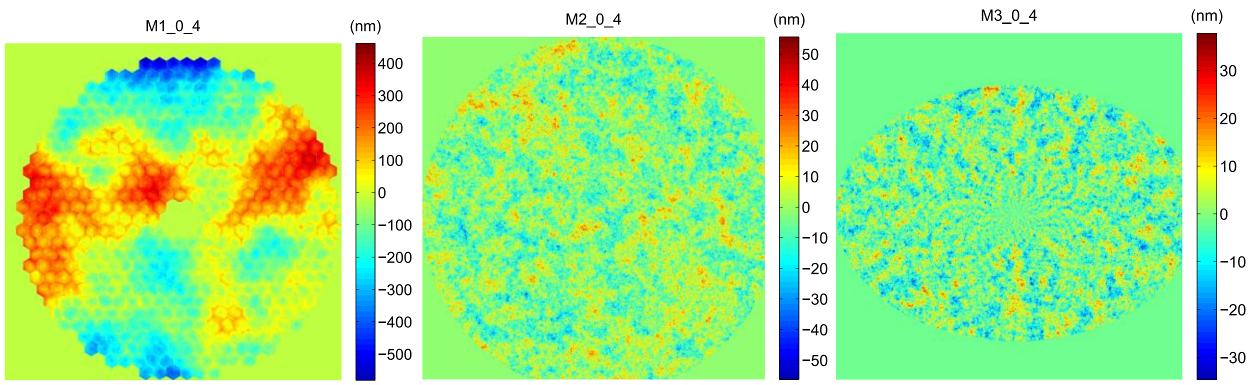

Figure 16: Left to right: TMT M1, M2, M3 wavefront errors (nm) at zenith pointing for a 4 deg temperature variation from the APS alignment temperature.

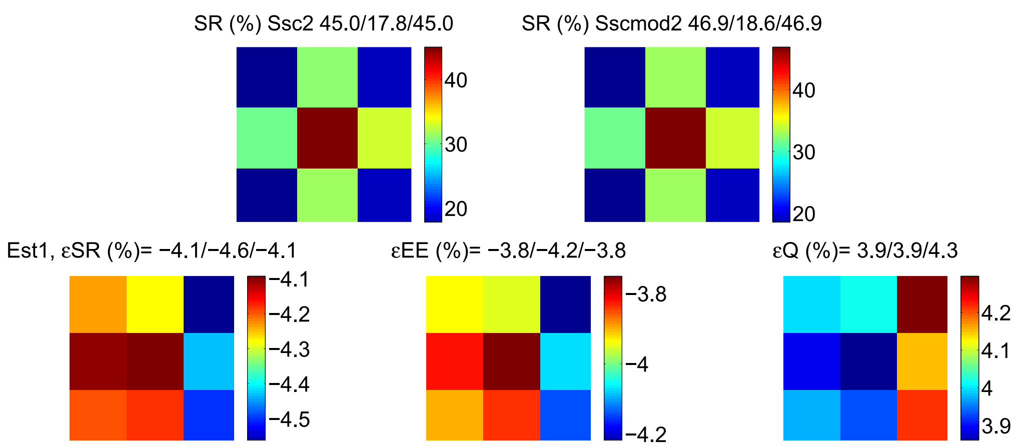

Figure 17: Top: Z-band SR at the 3 x 3 fields partitioning the 34'' x 34'' IRIS FoV (left image is for the system with the M1/M2/M3 OPDs, right image is for the simulation model excluding the M1/M2/M3 OPDs, and the three numbers in the title are the on-axis/min/max values across the 9 field points). Bottom: Z-band SR, EE and PSF profile errors for the 3 x 3 fields partitioning the FoV.

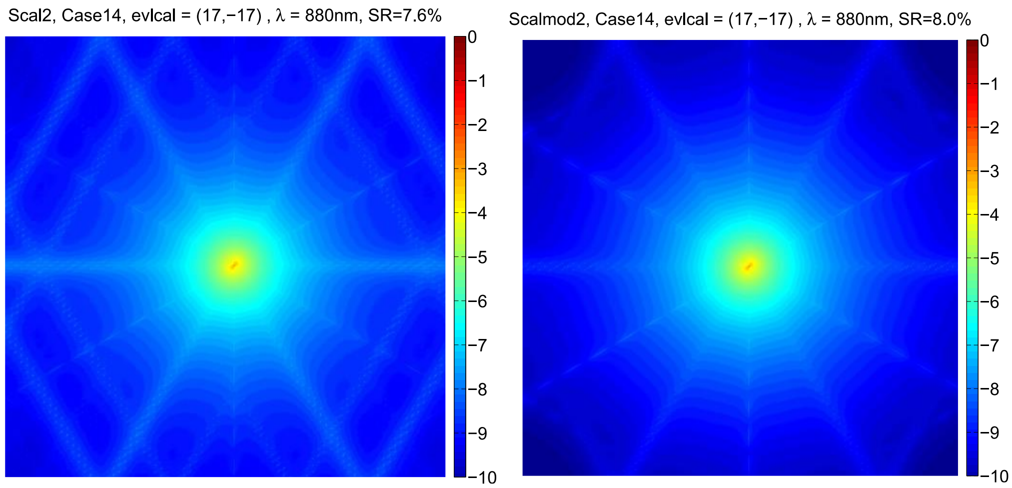

Figure 18: Left: Z-band Measured calibration PSF at coordinate (17'', -17'') (includes degradation due to M1/M2/M3 OPDs). Right: Z-band Calibration PSF model (excludes degradation due to M1/M2/M3 OPDs). Log10 scale.

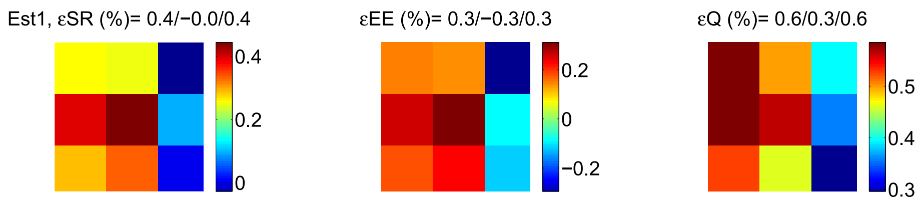

Figure 19: Z-band SR, EE and PSF profile errors for the 3 x 3 fields partitioning the 34'' x 34'' IRIS FoV with a calibration measurement performed at coordinate (17'', -17'') (upper right corner) at a different time than the science observation.

3. CONCLUSIONS

In this paper, a status update on PSFR algorithm development for LGS MCAO was provided. The estimation of the OTF degradation due to LGS WFS measurement noise, SLODAR turbulence profile estimation errors and static telescope errors was discussed for TMT NFIRAOS feeding the IRIS imager for various turbulence conditions. Off-axis, the quality of the reconstructed PSF is mostly impacted by the level of accuracy of the SLODAR algorithm. We have also pointed out that the variability of the PSF from one exposure to another for a given stationary frozen flow turbulence condition and a given exposure time places a fundamental limit on PSFR accuracy.

ACKNOWLEDGEMENTS

The authors gratefully acknowledge the support of the TMT collaborating institutions. They are the Association of Canadian Universities for Research in Astronomy (ACURA), the California Institute of Technology, the University of California, the National Astronomical Observatory of Japan, the National Astronomical Observatories of China and their consortium partners, and the Department of Science and Technology of India and their supported institutes. This work was supported as well by the Gordon and Betty Moore Foundation, the Canada Foundation for Innovation, the Ontario Ministry of Research and Innovation, the National Research Council of Canada, the Natural Sciences and Engineering Research Council of Canada, the British Columbia Knowledge Development Fund, the Association of Universities for Research in Astronomy (AURA), the U.S. National Science Foundation and the National Institutes of Natural Sciences of Japan.

REFERENCES

[1] L.Gilles, L.Wang and C.Boyer, "Point spread function reconstruction simulations for laser guide star multi-conjugate adaptive optics on extremely large telescopes", Proc. SPIE 10703 (2018), 12.2315793

[2] L.Gilles, L.Wang, M.Etsuko, J.P.Véran and C.Boyer, “Point spread function analysis, modeling, simulations and laboratory testing for TMT NFIRAOS”, Proc. AO4ELT5 (2017), doi:10.26698/AO4ELT5.0048
[3] C.Béchet, B.Ayancan, A.Guesalaga, C.Correia, B.Neichel, E.Masciadri and R.Conan “PSF reconstruction via full turbulence characterization end-to-end simulations”, Proc. AO4ELT5 (2017), doi:10.26698/AO4ELT5.0051
[4] A.Ciurlo, T.Do, G.Witzel, J.Lu, M.Fitzgerald and A.Ghez, “PSF reconstruction for integral field spectrograph OSIRIS at Keck”, Proc. AO4ELT5 (2017), doi:10.26698/AO4ELT5.0107
[5] R.Wagner, “PSF reconstruction and blind deconvolution for extremely large telescopes”, Durham PSFR workshop (2018).
[6] M.Schoeck and L.Gilles, “TMT PSF Reconstruction Status”, Durham PSFR workshop (2018).
[7] E.Por, “PSF reconstruction: phase sorting interferometry”, Durham PSFR workshop (2018).
[8] F.Cantalloube, “PSF reconstruction: dealing with the turbulence residual phase signature for high contrast imaging”, Durham PSFR workshop (2018).
[9] O.Beltramo-Martin, “Improving photometry and astrometry in crowded fields using PSF reconstruction”, Durham PSFR workshop (2018).
[10] O.Beltramo-Martin, C.Correia, E.Gendron, et al., “Point spread function reconstruction validated using on-sky Canary data in multiobject adaptive optics mode”, https://doi.org/10.1117/1.JATIS.2.4.048001 (2016).
[11] S.Ragland, T.Dupuy, L.Jolissaint, P.Wizinowich, et al. “Status of point spread function determination for Keck adaptive optics”, Proc. SPIE 10703 (2018), https://doi.org/10.1117/12.2312975
[12] L.Jolissaint, S.Ragland, J.Christou and P.Wizinowich, “Determination of the optical turbulence parameters from the adaptive optics telemetry: critical analysis and on-sky validation, Appl. Opt. 57, 7837-7856 (2018).
[13] J.Crane, G.Herriot, D.Andersen, J.Atwood et. al., “NFIRAOS adaptive optics for the Thirty Meter Telescope”, Proc. SPIE 10703 (2018), 10.1117/12.2314341
[14] Y.Hayano, R.Suzuki, M.Uchiyama et. al., “The infrared imaging spectrograph (IRIS) for TMT: status report for IRIS imager”, Proc. SPIE 10702 (2018), 10.1117/12.2314327
[15] K.Zhang, Y.Zhou, A.Moore et. al., “The infrared imaging spectrograph (IRIS) for TMT: design of image slicer”, Proc. SPIE 10702 (2018), 10.1117/12.2312700
[16] L.Gilles and B.Ellerebroek, “Real-time turbulence profiling with a pair of laser guide star Shack-Hartmann wavefront sensors for wide field adaptive optics systems on large to extremely large telescopes”, J.Opt.Soc.Am. A27, A76-A83 (2010).
[17] J. Goodman, “Introduction to Fourier Optics”, 2nd edition, McGraw-Hill (1996).
[18] F. Ferriera, E.Gendron, G.Rousset, D.Gratadour, “Numerical estimation of wavefront error breakdown in adaptive optics”, Astronomy & Astrophysics 616, A102 (2018), 10.1051/0004-6361/201832579
[19] B.-J. Seo, C. Nissly, M. Colavita, M. Troy, S. Roberts and J. Rogers, “Optical performance prediction of the Thirty Meter Telescope after initial alignment using optical modelling”, Proc. SPIE 10705 (2018), 10.1117/12.2314351
[20] L.Wang, MAOS, GitHub.
[21] L.Wang and B.Ellerbroek, “Computer simulations and real-time control of ELT AO systems using graphical processing units”, Proc. SPIE 8447 (2012), 10.1117/12.926500
[22] L.Gilles and B.Ellerbroek, “Split atmospheric tomography using laser and natural guide stars”, J.Opt.Soc.Am.A25, 2427-2435 (2008).
[23] O.Beltramo-Martin, C.Correia, E.Mieda, B.Neichel, T.Fusco, G.Witzel, J.Lu, J.P.Véran, “Off-axis point spread function characterization in laser guide star adaptive optics systems”, MNRAS 478, 4642-4656 (2018), doi:10.1093/mnras/sty1103.
[24] L.Gilles, L.Wang and B.L.Ellerbroek, "The impact of laser launch location on the performance of laser tomography and multi-conjugate adaptive optics for extremely large telescopes", Appl. Opt. 49, G114-G119 (2010).